Current-Driven Insulator-To-Metal Transition in Strongly Correlated VO_2

Yin Shi* and Long-Qing Chen†

Department of Materials Sciences and Engineering, Pennsylvania State University, University Park, Pennsylvania 16802, USA

(Received 30 October 2018; revised manuscript received 25 December 2018; published 29 January 2019)

Despite extensive studies on the insulator-to-metal transition (IMT) in strongly correlated VO_2, the fundamental mechanism underlying the current-driven IMT in VO_2 is still not well understood. Although it is generally believed that the mechanism is Joule heating leading to a rise in temperature to above the normal transition temperature, there is ample experimental evidence demonstrating that the transition could be driven by nonthermal electronic processes. Here we formulate a phase-field model to demonstrate that the electric current may drive the IMT isothermally via the current-induced electron-correlation weakening. We discover that a current with a large density (on the order of 10 $\mathrm{nA/nm^2}$) induces ultrafast resistive switching on the order of a few nanoseconds, consistent with experimental measurements. We also construct the temperature-current phase diagram and investigate the influence of the current on domain walls. This work is expected to provide guidance for understanding the current-driven IMT in VO_2 and for designing VO_2-based electric switching devices.

DOI: 10.1103/PhysRevApplied.11.014059

I. INTRODUCTION

The insulator-to-metal transition (IMT) in the strongly correlated electron system vanadium dioxide (VO_2) [1] has been attracting widespread attention; it not only provides a platform for fundamental scientific research of strong correlation physics [2–4] but also offers potential novel device applications such as sensors, Mott field-effect transistors, and memristors [5–9]. Above the transition temperature $T_c = 338$ K [10], VO_2 is a metal with a rutile (R) structure, while below T_c it turns into an insulator with a monoclinic (M1) structure, at which the resistivity, infrared transmission, and eigenstrain change dramatically [11,12]. Chemical doping [13] or the application of a uniaxial stress [14] can stabilize another monoclinic (M2) insulating phase. The IMT can be induced by various external stimuli, including temperature, strain or stress, doping, and light [1,13–15]. It has been experimentally demonstrated that the IMT can also be triggered by an electric voltage (field), which is of particular interest owing to its potential application in information technology [6–9,16].

Although the electric field alone (in an open circuit) can drive the IMT [6,16], the electric current commonly accompanying the electric field (in a closed circuit) may also lead to the IMT [17–21]. Unlike in the field-driven IMT where the initial insulating state changes to the equilibrium metallic ground state, in the current-driven IMT the insulating state changes to the nonequilibrium metallic steady state. Two kinetic processes are expected to occur simultaneously in VO_2 when it is subject to an electric current: the current heats up the system through Joule heating, and the free carriers injected into the system screen the electron-electron repulsion and thus reduce the electron correlation [22–24]. The Joule-heating effect can lead to a rise in temperature to above T_c and thus thermally trigger the IMT. On the other hand, the correlation-weakening effect induced by the current may delocalize the electrons in the insulating state, thereby inducing the IMT. These two mechanisms are often entangled with each other, complicating the understanding of the underlying mechanisms for the current-driven IMT.

Many experiments and simulations using dc biases and low-frequency voltage pulses seem to suggest that Joule heating is the main mechanism for the current-driven IMT [25–29]. For example, using the fluorescence spectra of rare-earth-doped micron-sized particles as local temperature sensors, Zimmers *et al.* [28] found that the local temperature of the VO_2 sample reaches the transition temperature T_c as the IMT is induced by a direct current. Nevertheless, other experiments showed that the transition voltage weakly depends on the thermal dissipation rate and the initial temperature of the VO_2 sample, indicating that the IMT is unlikely to be induced by the Joule-heating effect [30,31]. Furthermore, it has been found that the application of a voltage pulse of few volts (accompanied by a corresponding current pulse) switches VO_2 from an insulator to a metal in a few or tens of nanoseconds [17,19,20]. This ultrafast resistive switching can hardly be attributed to the Joule-heating mechanism since

*yxs187@psu.edu
†lqc3@psu.edu

the timescale of the Joule-heating-induced switching is expected to be at least 1 order of magnitude greater than the timescale of the switching observed in experiments [17,19,20]. According to these studies, the ultrafast switching must be driven primarily by the correlation-weakening effect induced by the current.

Despite extensive experimental studies on current-induced ultrafast switching, there are still no theoretical models that can be used to explore the mechanisms underlying the phenomenon. Recently we formulated a phase-field model to describe the IMT in VO_2. The thermodynamics is described by a Landau potential as a function of structural and electronic order parameters and free-electron and free-hole densities [32,33], which treats the structural distortion and the electron correlation on an equal footing. It has been successfully applied to the determination of equilibrium stable states under strain or stress [32], and under electric fields in an *open-circuit* configuration [33]. In this work, this model is further extended to describe the *nonequilibrium* process of the current-driven IMT in mesoscale systems (in a *closed-circuit* configuration). In particular, we formulate a kinetic model and apply it to the investigation of the current-driven IMT in VO_2 to explore the possibility of the IMT arising entirely from the electron-correlation weakening induced by the current; that is, we assume an isothermal situation, which may not be readily realized in real experiments. We demonstrate that the current can indeed drive the few-nanosecond ultrafast switching through the correlation-weakening effect. We further construct the temperature-current phase diagram and study the influence of the current on domain walls.

II. METHOD

The thermodynamics of the IMT in VO_2 can be described by a Landau-type potential-energy density functional [32,33],

$$F_t[T,\Phi;\{\eta_i\},\{\mu_i\},n,p] = F_0[T;\{\eta_i\},\{\mu_i\}] + F[T,\Phi;\{\mu_i\},n,p],$$

which consists of a contribution from the intrinsic VO_2, F_0, and a contribution from additional free carriers, F. Here T is the temperature, Φ is the electric potential, η_i ($i = 1,2,3,4$) are the structural-order-parameter fields, μ_i ($i = 1,2,3,4$) are the spin-correlation-order-parameter fields (characterizing the magnetic order), and n and p are the free-electron and free-hole density fields, respectively. η_i and μ_i explicitly characterize the structural and electronic phase transitions during the IMT, respectively: a finite η_i indicates the dimerization of the neighboring V atoms, and a finite μ_i indicates the formation of the dynamical singlet situated on the neighboring V sites and consequently the opening of the energy gap [2–4]. The order parameters of the different phases are $\eta_1 = \eta_3 \neq 0$, $\eta_2 = \eta_4 = 0$, $\mu_1 = \mu_3 \neq 0$, $\mu_2 = \mu_4 = 0$, $\eta_1\mu_1 < 0$, and $\eta_3\mu_3 < 0$ (and other symmetry-related values) for the M1 phase, $\eta_1 \neq 0$, $\eta_2 = \eta_3 = \eta_4 = 0$, $\mu_1 \neq 0$, $\mu_2 = \mu_3 = \mu_4 = 0$, and $\eta_1\mu_1 < 0$ (and other symmetry-related values) for the M2 phase, and $\eta_i = 0$ and $\mu_i = 0$ ($i = 1,2,3,4$) for the R phase [32]. The detailed form of the intrinsic Landau potential F_0 can be found in Refs. [32,33] and is also summarized in Appendix A. In previous work [33] we used the Boltzmann statistics commonly used in semiconductor physics as an approximation to the Fermi statistics for free electrons and holes. To better characterize the kinetics of the free electrons and holes, here we use the Fermi distribution to calculate the free-electron and free-hole densities.

Since the energy gap opens nearly symmetrically with respect to the Fermi level of the R phase during the metal-to-insulator transition [34], we can set the energy reference to the midpoint of the gap to simplify the description of the theory. With this reference and the simplification of one effective parabolic band for each of the conduction and valence bands, the electron and hole densities can be written as

$$n = N_c F_{1/2}\left(\frac{\xi_e - E_g/2 + e\Phi}{k_B T}\right), \tag{1a}$$

$$p = N_v F_{1/2}\left(\frac{\xi_h - E_g/2 - e\Phi}{k_B T}\right). \tag{1b}$$

Here the function $F_{1/2}(x) \equiv (2/\sqrt{\pi})\int_0^\infty \sqrt{\epsilon}[1+\exp(\epsilon - x)]^{-1}d\epsilon$ is the Fermi integral [35], k_B is the Boltzmann constant, and e is the elementary charge. $N_c = 2(m_e^* k_B T/2\pi\hbar^2)^{3/2}$ and $N_v = 2(m_h^* k_B T/2\pi\hbar^2)^{3/2}$ are the effective densities of states of the conduction band and the valence band, respectively, where m_e^* (m_h^*) is the effective mass of the electrons (holes) and $\hbar$ is the Planck constant divided by 2π [36]. ξ_e and ξ_h are the (quasi-) chemical potentials of the electrons and the holes, respectively. E_g is the gap, and may be directly related to the spin-correlation order parameters [2–4]: $E_g(\{\mu_i\}) \approx 2U^2\mu_0^2\sum_i \mu_i^2/k_B T_c$ (U is the on-site Coulomb repulsion and μ_0 is a dimensionless parameter) [32,33].

The free energy of the free electrons and holes is then just

$$F = \int\left[\int_0^n (\xi_e)_{TV} dn + \int_0^p (\xi_h)_{TV} dp\right] dV - F_i[T;\{\mu_i\}].$$

Using Eq. (1) to eliminate the chemical potentials, one obtains

$$F = \int\left\{k_B T\left[\int_0^n F_{1/2}^{-1}\left(\frac{n'}{N_c}\right)dn' + \int_0^p F_{1/2}^{-1}\left(\frac{p'}{N_v}\right)dp'\right] + \frac{E_g}{2}(n+p) + e\Phi(p-n)\right\} dV - F_i[T;\{\mu_i\}]. \tag{2}$$

Here $F_{1/2}^{-1}$ represents the inverse function of $F_{1/2}$ and V is the volume. F_i is the equilibrium intrinsic free energy of the electrons and holes, and thus F vanishes at equilibrium and zero electric field. F_i may have a complicated form. However, what is directly needed in the simulation is not F_i itself but $\delta F_i/\delta\mu_i$ [see Eq. (3)]. It can be proven (see Appendix B for the derivation) that $\delta F_i/\delta\mu_i = n_i dE_g/d\mu_i$, where $n_i = N_c F_{1/2}[(\xi_{\text{eq}} - E_g/2)/k_B T]$ is the intrinsic carrier density (ξ_{eq} is the equilibrium intrinsic chemical potential of the electrons).

The kinetics of the phase transition is described by the Allen-Cahn equations for the nonconserved order parameters η_i and μ_i [37],

$$\frac{\partial\eta_i}{\partial t} = -L_\eta\frac{\delta F_t}{\delta\eta_i}, \tag{3a}$$

$$\frac{\partial\mu_i}{\partial t} = -L_\mu\frac{\delta F_t}{\delta\mu_i}, \tag{3b}$$

and by the Cahn-Hilliard equations (diffusion equations) for the conserved order parameters n and p [37],

$$\frac{\partial n}{\partial t} = \nabla\cdot\left(\frac{M_e n}{e}\nabla\frac{\delta F_t}{\delta n}\right) + s, \tag{4a}$$

$$\frac{\partial p}{\partial t} = \nabla\cdot\left(\frac{M_h p}{e}\nabla\frac{\delta F_t}{\delta p}\right) + s, \tag{4b}$$

where t is the time, L_η and L_μ are constants related to the interface mobilities, M_e (M_h) is the electron (hole) mobility, and s is the source term representing the electron-hole recombination process. In Eqs. (3) and (4) the natural variables of F_t are $\{\eta_i\}$, $\{\mu_i\}$, T, V, n, and p, and $\delta F_t/\delta n = \xi_e$ and $\delta F_t/\delta p = \xi_h$.

The source term may have the form $s = K(\{\mu_i\})(n_{\text{eq}}p_{\text{eq}} - np)$, where $n_{\text{eq}} = N_c F_{1/2}[(\xi_{\text{eq}} - E_g/2 + e\Phi)/k_B T]$ and $p_{\text{eq}} = N_v F_{1/2}[(-\xi_{\text{eq}} - E_g/2 - e\Phi)/k_B T]$ are the equilibrium densities of the electrons and the holes, respectively, and K is the recombination-rate coefficient independent of n and p. In the insulating phase, K is finite. In the metallic phase, however, K should be zero: the holes appearing in the metallic phase in the model are not genuine holes as in the insulating phase, but rather should be interpreted as an effective positive-charge background for the free electrons to achieve charge neutrality, in which case the concept of electron-hole recombination is not applicable. To account for this, we assume the symmetry-allowed lowest-order dependence of K on the electronic order parameters, $K = K_0\sum_i \mu_i^2$, where K_0 is a constant.

Equations (3) and (4) are closed by the Poisson equation for the self-consistent determination of the electric potential Φ,

$$-\nabla^2\Phi = \frac{e(p-n)}{\epsilon_0\epsilon_r},$$

where ϵ_0 and ϵ_r are the vacuum dielectric permittivity and the relative dielectric permittivity of VO_2, respectively. In the simulations, for Eq. (4) we use the energies $\gamma_e \equiv \xi_e - E_g/2 + e\Phi$ and $\gamma_h \equiv \xi_h - E_g/2 - e\Phi$ as the unknown variables instead of n and p, and obtain n and p through Eq. (1) after solving for γ_e and γ_h.

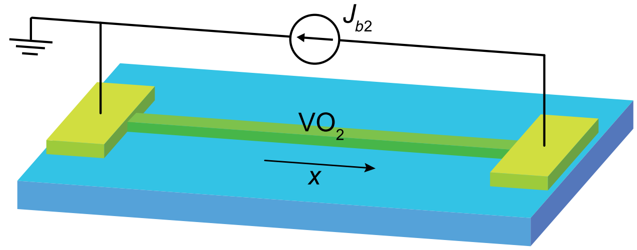

FIG. 1. The geometry used in the simulations. The blue and the gold parts are the substrate and electrodes, respectively. The length of the VO_2 sample is L and is set to 100 nm in the simulations.

The boundary conditions are schematically represented in Fig. 1. The left boundary ($x = 0$) is connected to the ground; that is, we have

$$\Phi|_{x=0} = 0,$$
$$\gamma_e|_{x=0} = \gamma_h|_{x=0} = \gamma_{\text{b1}},$$

where γ_{b1} is a constant corresponding to a fixed carrier density n_{b1} at the boundary, $n|_{x=0} = p|_{x=0} = n_{\text{b1}}$. The right boundary ($x = L$) has a constant flux. We assume that the boundary condition for Φ at $x = L$ corresponds to a small constant electric field in the electrode E_{lctrd2} (we set E_{lctrd2} to 0.001 MV/m). Eventually we have

$$(\partial_x\Phi)|_{x=L} + E_{\text{lctrd2}} = \frac{e(p-n)|_{x=L}\lambda}{\epsilon_0\epsilon_r},$$
$$j_e|_{x=L} = -\frac{J_{\text{b2}}}{e},\ j_h|_{x=L} = 0,$$

where λ is the length of the charge-depletion region at the boundary and is set to 5 nm, $j_e = -(M_e n/e)\partial_x\xi_e$ is the electron flux, $j_h = -(M_h p/e)\partial_x\xi_h$ is the hole flux, and J_{b2} is the constant boundary current density. In the simulations we find that different values of E_{lctrd2} and λ have a minor influence on the results. We assume a Neumann boundary condition for the order parameters η_i and μ_i at both boundaries—that is, $(\partial_x\eta_i)|_{x=0,L} = (\partial_x\mu_i)|_{x=0,L} = 0$—which corresponds to no interaction of the order parameters at boundaries.

We estimate the parameters in the model on the basis of experimental results. To the best of our knowledge, the

TABLE I. Values of the parameters estimated from experiments.

m_e^*, m_h^* (m_e)[a] [38]	M_e (cm^2/V s) [39]	M_e/M_h [34]	K_0 (cm^3/s) [34]	L_η (cm^3/J s) [15]	L_μ (cm^3/J s) [24]	ϵ_r[b] [40]
65	0.5	1.2	6.8×10^{-17}	3.3×10^{10}	2.0×10^{11}	60

[a] m_e is the electron mass.
[b] ϵ_r varies appreciably with temperature. However we observe that different values of ϵ_r have a minor influence on the switching behavior; for example, the switching times for $\epsilon_r \sim 40$ (near room temperature) and for $\epsilon_r \sim 100$ (near 320 K) at a temperature of 320 K and a current density of 57.8 nA/nm^2 differ within 2%.

hole mobility in VO_2 has not yet been directly measured. Nonetheless, we estimate the ratio of the electron and hole mobilities $M_e/M_h \approx 1.2$ from the position of the photocurrent peak in the scanning-photocurrent-microscopy measurement [34]. The constant characterizing the electron-hole recombination rate K_0 can be calculated from the free-carrier lifetime $\tau_{e\text{-}h} \sim 10\ \mu$s [34] through the relation $K_0 = (2n_{\text{ic}}\tau_{e\text{-}h})^{-1}$ [41], where n_{ic} is the intrinsic carrier density of the insulating phase near T_c (note that $\sum_i \mu_i^2 \sim 1$ in the insulating phase). Similarly, L_η and L_μ can be estimated from the characterization times of the structural and the electronic phase transitions, $\tau_\eta \sim 1$ ps [15] and $\tau_\mu \sim 10$ fs [24], by $L_\eta \sim [\tau_\eta a(T_c - T_1)/T_c]^{-1}$ and $L_\mu \sim (4U^2\mu_0^2 n_{\text{ex}}\tau_\mu/k_B T_c)^{-1}$, respectively. Here a and T_1 are the Landau coefficient and the Curie-Weiss temperature of the quadratic term of η_i, respectively (see Appendix A), and $n_{\text{ex}} \approx 0.08$ per V atom is the photoexcited-free-electron density in the measurement of τ_μ [24]. The values of the parameters estimated from experiments are summarized in Table I.

III. CURRENT-DRIVEN ULTRAFAST SWITCHING AND PHASE DIAGRAM

We first investigate the case in which the VO_2 sample has an initial equilibrium M1 phase in the bulk and is subject to a large current density on the order of 10 nA/nm^2. This could be the case in measurements of the voltage-pulse-induced ultrafast switching in VO_2 [17,19,20]. Figure 2 shows the calculated temporal evolution of various variables at $T = 320$ K, $J_{\text{b2}} = 57.8$ nA/nm^2, and $n_{\text{b1}} \approx 0.6$ per unit cell. We find that n_{b1} has a minor influence on the profiles of the variables in the bulk and on the switching time. At $t = 0$ ns, the structural order parameters and the electronic order parameters have uniform equilibrium finite values $\eta_1 = \eta_3 = 0.76$ and $\mu_1 = \mu_3 = -0.84$ in the bulk ($\eta_2 = \eta_4 = 0$ and $\mu_2 = \mu_4 = 0$), indicating the initial state is a uniform monoclinic insulator (M1 phase). η_1 (η_3) and μ_1 (μ_3) then become zero from the $x = L$ end, representing that the rutile metal (R phase) grows from the $x = L$ end. This is in contrast to the Joule-heating-induced switching, in which the initial insulator turns into the metal uniformly due to the uniform heating. The metallic phase spreads from the $x = L$ end to the $x = 0$ end in approximately 9 ns, yielding a few-nanosecond ultrafast switching. This is consistent with the 4-ns switching time (scaled to a 100-nm-long VO_2 sample) observed in the voltage-pulse-induced IMT in VO_2 at a peak current density on the order of 10–100 nA/nm^2 [17].

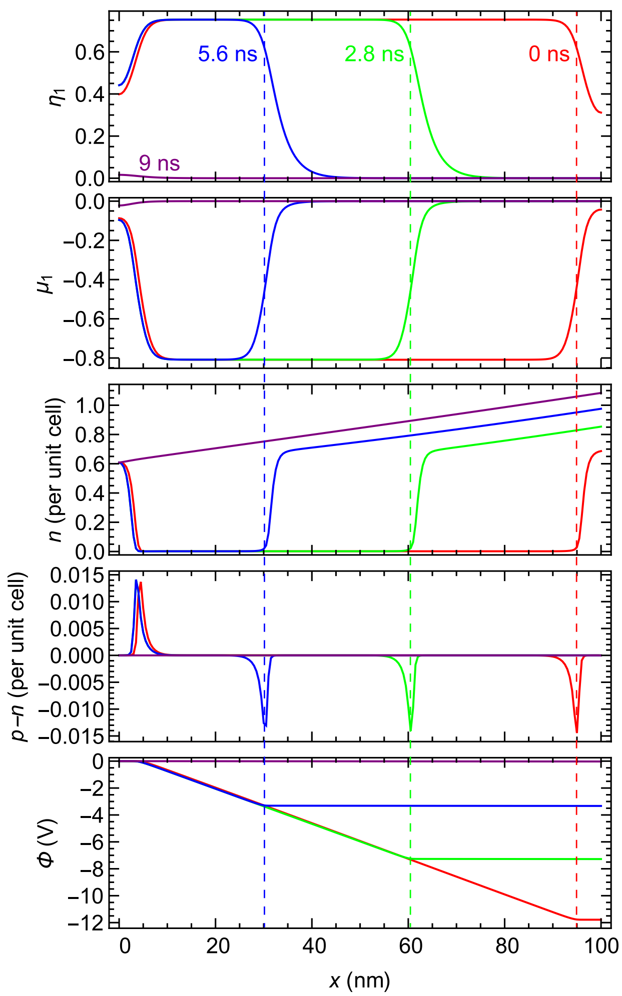

FIG. 2. Simulated temporal evolution of various variables during the current-driven ultrafast switching in VO_2 at $T = 320$ K, $J_{\text{b2}} = 57.8$ nA/nm^2, and $n_{\text{b1}} \approx 0.6$ per unit cell. During the process, η_3 (μ_3) is the same as η_1 (μ_1), and $\eta_2 = \eta_4 = 0$ and $\mu_2 = \mu_4 = 0$. The dashed lines indicate the positions of the insulator-metal interface at different times.

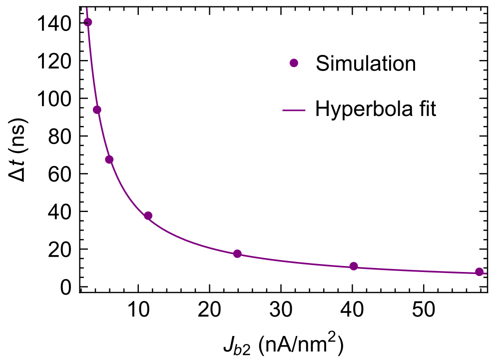

FIG. 3. Switching time as a function of the current density in VO_2 at $T = 320$ K. The line is the hyperbola fit to the simulation data, $\Delta t = c/J_{b2}$, with the fitted constant $c = 412$ ns nA/nm^2.

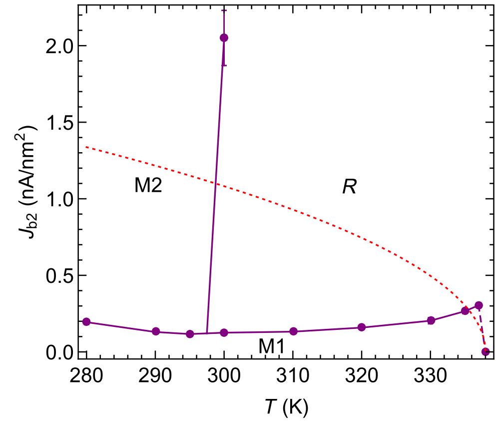

FIG. 4. Calculated temperature-versus-current-density phase diagram of VO_2. The dots with error bars are the calculated points on the phase boundaries (the presence of the error bars results from the discretely sampled calculation points on the phase diagram), and the lines are a guide for the eye. The dashed line represents the discontinuous point. The dotted red line is the boundary line for the Joule-heating-induced IMT: for J_{b2} exceeding this line, the R phase will eventually be induced by the Joule-heating effect (see the text).

Compared with the IMT induced by the photoexcited electrons in the optical experiments [15,24], the growth of the metallic phase from the $x = L$ end is driven by the carrier doping from the carrier injection and the negative electric potential [6,33]. The excess carriers screen the electron-electron repulsion and thus reduce the electron correlation (the electronic order parameters), thereby stabilizing the metallic phase [22–24]. As the metallic phase grows, net negative charges accumulate at the insulator-metal interface. The electric potential becomes flat inside the metallic phase as expected.

The switching time Δt depends on the current density. Figure 3 presents Δt as a function of the applied current density J_{b2}, showing that Δt decreases as J_{b2} increases. $\Delta t(J_{b2})$ is well fitted by a hyperbolic function, $\Delta t = c/J_{b2}$, with $c = 412$ ns nA/nm^2. Since the metallic phase grows from one end to another, J_{b2} is proportional to the average growth speed of the metallic phase, implying that the switching is controlled by the carrier dynamics (not the phase-transformation dynamics). It can be interpreted by the fact that the characteristic times of the electronic and structural phase transitions τ_μ and τ_η, are much shorter than the time for the carrier density at the metal-insulator interface to reach the metallic value, τ_0. τ_0 can be estimated to be $\tau_0 \approx d_0/v_0 \approx 0.4$ ns, which is indeed much longer than τ_μ and τ_η, where $v_0 \approx 13$ m/s is the average growth speed of the metallic phase and $d_0 \approx 5$ nm is half of the interface width (see Fig. 2). This further implies that the switching behavior is insensitive to τ_η and τ_μ as long as τ_η and τ_μ do not vary by many orders of magnitude. The fitting function can be used to calculate the switching time at large current densities; for example, $\Delta t = 0.2$ ns at $J_{b2} = 2 \times 10^3$ nA/nm^2, which is comparable to the 0.48-ns switching time (scaled to a 100-nm-long VO_2 sample) found in the voltage-pulse-induced IMT in VO_2 at a peak current density of the same magnitude [19].

Knowing that the current can induce the IMT isothermally, we further calculate the temperature-versus-current-density phase diagram of VO_2 under the isothermal condition. The result is shown in Fig. 4. Any point on the phase diagram corresponds to a nonequilibrium steady state, not an equilibrium stable state. Strikingly, the simulation suggests that the current may induce the M2 phase at low temperatures (below 298 K). The M2-R phase boundary has a large positive slope, indicating that a current with large enough density may eventually drive the M1 phase to the M2 phase even at high temperatures (above 298 K).

Nonetheless, in practice the Joule-heating effect may set a boundary line in the phase diagram, beyond which it governs the IMT. The criterion for the onset of the Joule-heating-induced IMT depends on the sample geometry and heat dissipation to the surroundings. For the geometry shown in Fig. 1, we consider that the heat generated in VO_2 is mainly dissipated through the substrate. At the steady state, the critical current density for the onset of the Joule-heating-induced IMT J_{Jc} is simply determined by the balance between the electric power and the heat dissipation,

$$\frac{J_{Jc}^2}{\sigma} = \frac{h}{D}(T_c - T_s), \tag{5}$$

where $\sigma = 4.6 \times 10^3$ S/m is the conductivity of the insulating phase of VO_2 at T_c [42], $h \sim 6.7 \times 10^5$ W/Km^2 is the effective heat transfer coefficient for a 100-nm-thick VO_2 film in contact with a sapphire substrate [27], D is the thickness of the VO_2 nanobeam (perpendicular to the substrate plane), and T_s is the temperature of the substrate (also considered as the initial temperature of the VO_2 sample). J_{Jc} as a function of T_s from Eq. (5) for a typical

$D = 100$ nm is plotted in Fig. 4 as a dotted red line. Therefore, in a typical 100-nm-thick VO_2 film or nanobeam on a sapphire substrate, the Joule heating will eventually induce the R phase for J_{b2} exceeding the boundary line $J_{Jc}(T_s)$. For polycrystalline VO_2, J_{Jc} could be dramatically suppressed due to the suppressed conductivity.

The critical current density of the M1-R phase transition increases at elevated temperature, which finally leads to the presence of a discontinuous point at T_c, as shown by the dashed line in Fig. 4. This may be interpreted as follows. The growth of the metallic phase is driven by the carrier accumulation at the metal-insulator interface. At the insulator side, a higher temperature (below T_c) leads to a higher carrier density, resulting in a larger current density there. Hence, for free electrons to accumulate at the metal-insulator interface at a higher temperature, the current density must be larger at the metal side (exceeding the current density at the insulator side). In practice the discontinuous point in the phase diagram should not be present. When the temperature approaches T_c, J_{Jc} will be smaller than the critical J_{b2} (Fig. 4), meaning that the Joule-heating effect controls the IMT there. Thus, the critical current density will practically follow J_{Jc} and drop to zero continuously when $T \to T_c$.

IV. CURRENT-DRIVEN DOMAIN-WALL MOTION

We now examine how the current affects the domain wall in VO_2. The initial configuration is set to a two-domain structure within the M1 phase, with the domain wall (twin wall) located at $x = L/2$. This is shown by the profiles of η_3 and μ_3 at $t = 0$ ns in Fig. 5. The order parameters of the right domain are $\eta_1 = \eta_3 = 0.76$, $\eta_2 = \eta_4 = 0$, $\mu_1 = \mu_3 = -0.84$, and $\mu_2 = \mu_4 = 0$, which is denoted as variant 1 of the M1 phase. The order parameters of the left domain are $\eta_1 = -\eta_3 = 0.76$, $\eta_2 = \eta_4 = 0$, $\mu_1 = -\mu_3 = -0.84$, and $\mu_2 = \mu_4 = 0$, which corresponds to a 180° rotation about the rutile c axis of variant 1, and is denoted as variant 3 of the M1 phase. As can be seen in Fig. 5, on the application of a current with a small density (not adequate to trigger the IMT), the twin wall between variant 1 and variant 3 moves oppositely to the current direction (i.e., $-x$ direction), and finally moves to the $x = 0$ end in less than 27 ns, leading to the vanishing of variant 3.

The twin wall has a relatively large carrier density and thus a relatively large conductivity compared with the interior of the domains. The net charges localized at the twin wall form an effective dipole oriented along the direction of the electric field. For the same reason as discussed for the current-driven switching, the twin-wall motion speed is insensitive to τ_μ and τ_η.

Similarly to the current-driven resistive switching, the current density affects the speed of the twin-wall motion. Figure 6 shows the average speed, v, of the twin-wall motion from $x = 50$ nm to $x = 0$ nm as a function of the current density. First v increases and it then decreases as the current density increases. It reaches its maximum at $J_{b2} \sim 0.026$ nA/nm^2 and approaches zero when J_{b2} approaches the critical value for triggering the IMT. The reason why v decreases with increasing J_{b2} at large J_{b2} is as follows. v should be proportional to the carrier accumulation rate in front of the twin wall, $v \propto (\partial_t n)|_{x_0-d/2}$, where x_0 denotes the position of the twin wall and d is the twin-wall thickness. But we have $(\partial_t n)|_{x_0-d/2} \sim -2[j_e(x_0) - j_e(x_0 - d/2)]/d$, where $j_e \sim -M_e n E$ (E is the electric field). Hence, $(\partial_t n)|_{x_0-d/2} \sim 2M_e[n(x_0)E(x_0) - n(x_0 - d/2)E(x_0 - d/2)]/d$. From the Poisson equation, the electric fields at x_0 and $x_0 - d/2$ have the relation

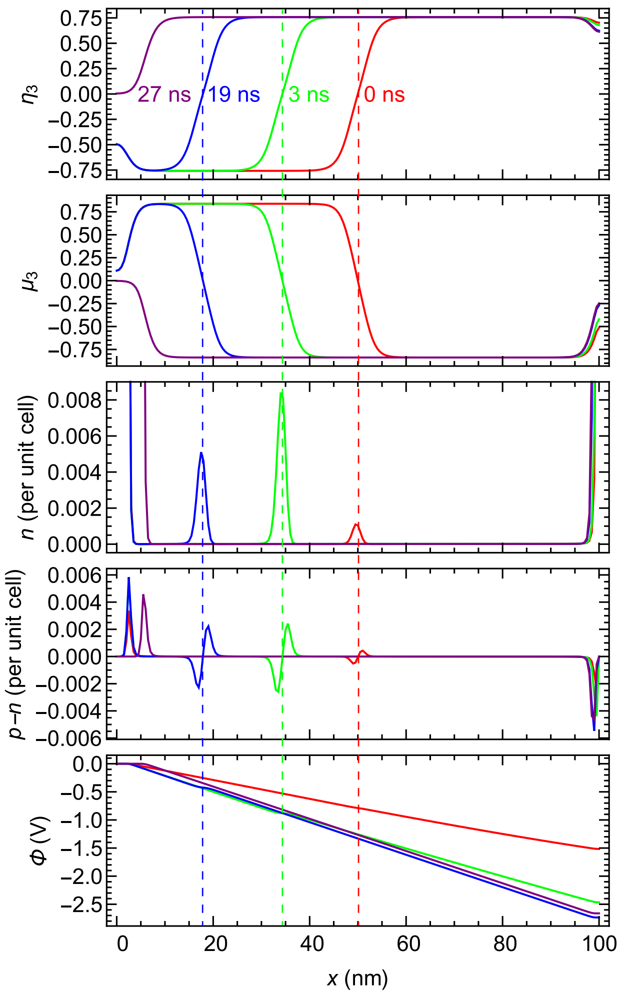

FIG. 5. Simulated temporal evolution of various variables during the current-driven domain-wall motion in VO_2 at $T = 320$ K, $J_{b2} = 0.0811$ nA/nm^2, and $n_{b1} \approx 0.6$ per unit cell. During the process, η_1 (μ_1) has a nearly uniform value of 0.76 (−0.84) along the sample except at the boundaries, and $\eta_2 = \eta_4 = 0$ and $\mu_2 = \mu_4 = 0$. The dashed lines indicate the positions of the twin wall within the M1 phase at different times. The range of the finite net-charge region at the $x = L$ boundary is within $\lambda \triangleq 5$ nm, which justifies this setting of λ.

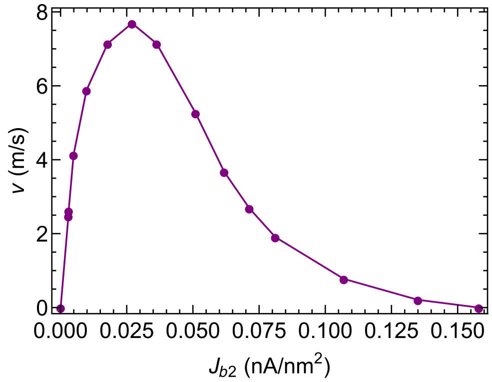

FIG. 6. Average speed of the twin-wall motion from $x = 50$ nm to $x = 0$ nm as a function of the current density in VO_2 at $T = 320$ K. The line is a guide for the eye.

$2[E(x_0) - E(x_0 - d/2)]/d \approx \rho_0/\epsilon_0\epsilon_r$, where $\rho_0 < 0$ is the net charge density at $x_0 - d/2$ (see the $p - n$ profile in Fig. 5). Then we have

$$v \propto \left[n(x_0) - n\left(x_0 - \frac{d}{2}\right)\right] E\left(x_0 - \frac{d}{2}\right) + \frac{n(x_0)\rho_0 d}{2\epsilon_0\epsilon_r}.$$

The increasing J_{b2} leads to an increase in $E(x_0 - d/2)$ [note that $n(x_0) - n(x_0 - d/2) > 0$], while the increased electric field leads to a stronger electron-hole separation near the twin wall, thus resulting in a smaller ρ_0 (more negative). These two competing effects lead to the eventual drop of v as J_{b2} increases.

This current-driven twin-wall motion cannot be realized via the Joule-heating effect since the Joule-heating effect is symmetric about the x and $-x$ directions.

V. CONCLUSION

We formulate a phase-field model that takes into account the structural distortion, the electron correlation, and the free carriers to describe the mesoscale kinetics of the IMT in strongly correlated VO_2. We apply it to the investigation of the isothermal current-driven IMT in VO_2. The simulation shows that the free electrons injected by a current with large density reduce the electron correlation (electronic order parameter μ_i) and lead to a few-nanosecond ultrafast resistive switching isothermally. The temperature-versus-current-density phase diagram obtained indicates that the current may induce the M2 phase at low temperatures under the isothermal condition. The current is also shown to be able to drive the domain wall to move, which could potentially be used to transform a multidomain sample to the single-domain state. This theoretical framework could be used to simulate other phase-transition processes in mesoscale VO_2 systems subject to various external stimuli, and may be extended to other strongly correlated materials exhibiting IMT.

ACKNOWLEDGMENTS

This work was funded by the Pennsylvania State University Center for Nanoscale Science, a Materials Research Science and Engineering Center, under NSF Grant No. DMR-1420620.

APPENDIX A: EXPRESSION FOR F_0

The intrinsic Landau potential F_0 consists of a bulk energy term f_b and a gradient energy term f_g [32,33],

$$F_0 = \int [f_b(T; \{\eta_i\}, \{\mu_i\}) + f_g(\{\eta_i\}, \{\mu_i\})]dV,$$

where dV is the infinitesimal volume element. f_b can be constructed from symmetry analysis [32],

$$\begin{aligned} f_b = {} & \frac{a(T - T_1)}{2T_c}\eta_i\eta_i + \frac{b_{ij}}{4}\eta_i^2\eta_j^2 + \frac{c_{ij}}{6}\eta_i^2\eta_j^4 \\ & + \frac{A(T - T_2)}{2T_c}\mu_i\mu_i + \frac{B_{ij}}{4}\mu_i^2\mu_j^2 + \frac{C_{ij}}{6}\mu_i^2\mu_j^4 \\ & + h\eta_i\mu_i - \frac{p_{ijkl}}{2}\eta_i\eta_j\mu_k\mu_l + \frac{q_{ijkl}}{2}\eta_i\eta_j\eta_k\mu_l, \end{aligned}$$

where T_1 and T_2 are the Curie-Weiss temperatures of the structural and electronic order parameters, respectively, and a, b_{ij}, c_{ij}, A, B_{ij}, C_{ij}, h, p_{ijkl}, and q_{ijkl} are constants satisfying certain symmetry relations [32]. The Einstein summation convention is used. We assume an isotropic form for f_g [33,43],

$$f_g = \frac{\kappa_1}{2}(\nabla\eta_i)\cdot(\nabla\eta_i) + \frac{\kappa_2}{2}(\nabla\mu_i)\cdot(\nabla\mu_i),$$

where κ_1 and κ_2 are positive constants.

APPENDIX B: DERIVATION OF $\delta F_i/\delta\mu_i$

Let us first denote the integral in Eq. (2) at $\Phi = 0$ as $F^0[\{\mu_i\}, n, p]$. Then by definition $F_i[\{\mu_i\}] = F^0|_{n,p=n_i}$. Since F_i depends on μ_i only through $E_g(\{\mu_i\})$, we obtain

$$\frac{\delta F_i}{\delta\mu_i} = \frac{\delta F_i}{\delta E_g}\frac{dE_g}{d\mu_i}. \tag{B1}$$

We also have

$$\frac{\delta F_i}{\delta E_g} = \frac{\delta F^0}{\delta E_g}\bigg|_{n,p=n_i} + \left(\frac{\delta F^0}{\delta n} + \frac{\delta F^0}{\delta p}\right)\bigg|_{n,p=n_i}\frac{dn_i}{dE_g}.$$

But $(\delta F^0/\delta E_g)|_{n,p=n_i} = n_i$, and the equilibrium conditions are $(\delta F^0/\delta n)|_{n,p=n_i} = \xi_e = \xi_{eq}$ and $(\delta F^0/\delta p)|_{n,p=n_i} =$

$\xi_h = -\xi_{eq}$ [33]. We thus have

$$\frac{\delta F_i}{\delta E_g} = n_i.$$

The substitution of this equation in Eq. (B1) gives the desired relation

$$\frac{\delta F_i}{\delta \mu_i} = n_i \frac{dE_g}{d\mu_i}.$$

This completes the proof.

[1] F. J. Morin, Oxides Which Show a Metal-to-Insulator Transition at the Neel Temperature, Phys. Rev. Lett. **3**, 34 (1959).

[2] S. Biermann, A. Poteryaev, A. I. Lichtenstein, and A. Georges, Dynamical Singlets and Correlation-Assisted Peierls Transition in VO_2, Phys. Rev. Lett. **94**, 026404 (2005).

[3] Huihuo Zheng and Lucas K. Wagner, Computation of the Correlated Metal-Insulator Transition in Vanadium Dioxide from First Principles, Phys. Rev. Lett. **114**, 176401 (2015).

[4] W. H. Brito, M. C. O. Aguiar, K. Haule, and G. Kotliar, Metal-Insulator Transition in VO_2: A DFT + DMFT Perspective, Phys. Rev. Lett. **117**, 056402 (2016).

[5] Feiyi Liao, Zheng Zhu, Zhuocheng Yan, Guang Yao, Zhenlong Huang, Min Gao, Taisong Pan, Yin Zhang, Qiang Li, Xue Feng, and Yuan Lin, Ultrafast response flexible breath sensor based on vanadium dioxide, J. Breath. Res. **11**, 036002 (2017).

[6] M. Nakano, K. Shibuya, D. Okuyama, T. Hatano, S. Ono, M. Kawasaki, Y. Iwasa, and Y. Tokura, Collective bulk carrier delocalization driven by electrostatic surface charge accumulation, Nature **487**, 459 (2012).

[7] Myungwoo Son, Joonmyoung Lee, Jubong Park, Jungho Shin, Godeuni Choi, Seungjae Jung, Wootae Lee, Seonghyun Kim, Sangsu Park, and Hyunsang Hwang, Excellent selector characteristics of nanoscale VO_2 for high-density bipolar ReRAM applications, Electron Device Lett. IEEE **32**, 1579 (2011).

[8] T. Driscoll, H.-T. Kim, B.-G. Chae, M. Di Ventra, and D. N. Basov, Phase-transition driven memristive system, Appl. Phys. Lett. **95**, 043503 (2009).

[9] Zheng Yang, Changhyun Ko, and Shriram Ramanathan, Oxide electronics utilizing ultrafast metal-insulator transitions, Annu. Rev. Mater. Res. **41**, 337 (2011).

[10] Jae Hyung Park, Jim M. Coy, T. Serkan Kasirga, Chunming Huang, Zaiyao Fei, Scott Hunter, and David H. Cobden, Measurement of a solid-state triple point at the metal-insulator transition in VO_2, Nature **500**, 431 (2013).

[11] A. Zylbersztejn and N. F. Mott, Metal-insulator transition in vanadium dioxide, Phys. Rev. B **11**, 4383 (1975).

[12] Elizabeth E. Chain, Optical properties of vanadium dioxide and vanadium pentoxide thin films, Appl. Opt. **30**, 2782 (1991).

[13] M. Marezio, D. B. McWhan, J. P. Remeika, and P. D. Dernier, Structural aspects of the metal-insulator transitions in Cr-doped VO_2, Phys. Rev. B **5**, 2541 (1972).

[14] J. P. Pouget, H. Launois, J. P. D'Haenens, P. Merenda, and T. M. Rice, Electron Localization Induced by Uniaxial Stress in Pure VO_2, Phys. Rev. Lett. **35**, 873 (1975).

[15] A. Cavalleri, Cs. Tóth, C. W. Siders, J. A. Squier, F. Ráksi, P. Forget, and J. C. Kieffer, Femtosecond Structural Dynamics in VO_2 during an Ultrafast Solid-Solid Phase Transition, Phys. Rev. Lett. **87**, 237401 (2001).

[16] B. Wu, A. Zimmers, H. Aubin, R. Ghosh, Y. Liu, and R. Lopez, Electric-field-driven phase transition in vanadium dioxide, Phys. Rev. B **84**, 241410 (2011).

[17] J. Leroy, A. Crunteanu, A. Bessaudou, F. Cosset, C. Champeaux, and J.-C. Orlianges, High-speed metal-insulator transition in vanadium dioxide films induced by an electrical pulsed voltage over nano-gap electrodes, Appl. Phys. Lett. **100**, 213507 (2012).

[18] Giwan Seo, Bong-Jun Kim, Changhyun Ko, Yanjie Cui, Yong Lee, Jun-Hwan Shin, Shriram Ramanathan, and Hyun-Tak Kim, Voltage-pulse-induced switching dynamics in VO_2 thin-film devices on silicon, Electron Device Lett. IEEE **32**, 1582 (2011).

[19] You Zhou, X. N. Chen, C. H. Ko, Zheng Yang, Chandra Mouli, and Shriram Ramanathan, Voltage-triggered ultrafast phase transition in vanadium dioxide switches, IEEE Electron Device Lett. **34**, 220 (2013).

[20] Byung-Gyu Chae, Hyun-Tak Kim, Doo-Hyeb Youn, and Kwang-Yong Kang, Abrupt metal–insulator transition observed in VO_2 thin films induced by a switching voltage pulse, Physica B: Condens. Matter **369**, 76 (2005).

[21] Yoshiaki Taketa and Ryoichi Furugochi, Switching and oscillation phenomena in SnO_2-VO_x-PdO ceramics, Appl. Phys. Lett. **31**, 405 (1977).

[22] Hyun-Tak Kim, Byung-Gyu Chae, Doo-Hyeb Youn, Sung-Lyul Maeng, Gyungock Kim, Kwang-Yong Kang, and Yong-Sik Lim, Mechanism and observation of Mott transition in VO_2-based two-and three-terminal devices, New J. Phys. **6**, 52 (2004).

[23] G. Stefanovich, A. Pergament, and D. Stefanovich, Electrical switching and Mott transition in VO_2, J. Phys.: Condens. Matter **12**, 8837 (2000).

[24] Daniel Wegkamp, Marc Herzog, Lede Xian, Matteo Gatti, Pierluigi Cudazzo, Christina L. McGahan, Robert E. Marvel, Richard F. Haglund, Angel Rubio, Martin Wolf, and Julia Stähler, Instantaneous Band Gap Collapse in Photoexcited Monoclinic VO_2 due to Photocarrier Doping, Phys. Rev. Lett. **113**, 216401 (2014).

[25] Bongjin Simon Mun, Joonseok Yoon, Sung-Kwan Mo, Kai Chen, Nobumichi Tamura, Catherine Dejoie, Martin Kunz, Zhi Liu, Changwoo Park, Kyungsun Moon, and Honglyoul Ju, Role of Joule heating effect and bulk-surface phases in voltage-driven metal-insulator transition in VO_2 crystal, Appl. Phys. Lett. **103**, 061902 (2013).

[26] Iuliana P. Radu, B. Govoreanu, S. Mertens, X. Shi, M. Cantoro, M. Schaekers, M. Jurczak, Stefan De Gendt, Andre Stesmans, J. A. Kittl, M. Heyns, and K. Martens, Switching mechanism in two-terminal vanadium dioxide devices, Nanotechnology **26**, 165202 (2015).

[27] S. B. Lee, K. Kim, J. S. Oh, B. Kahng, and J. S. Lee, Origin of variation in switching voltages in threshold-switching phenomena of VO_2 thin films, Appl. Phys. Lett. **102**, 063501 (2013).

[28] A. Zimmers, L. Aigouy, M. Mortier, A. Sharoni, Siming Wang, K. G. West, J. G. Ramirez, and Ivan K. Schuller, Role of Thermal Heating on the Voltage Induced Insulator-Metal Transition in VO_2, Phys. Rev. Lett. **110**, 056601 (2013).

[29] Dasheng Li, Abhishek A. Sharma, Darshil K. Gala, Nikhil Shukla, Hanjong Paik, Suman Datta, Darrell G. Schlom, James A. Bain, and Marek Skowronski, Joule heating-induced metal–insulator transition in epitaxial VO_2/TiO_2 devices, ACS. Appl. Mater. Interfaces **8**, 12908 (2016).

[30] Arash Joushaghani, Junho Jeong, Suzanne Paradis, David Alain, J. Stewart Aitchison, and Joyce K. S. Poon, Voltage-controlled switching and thermal effects in VO_2 nano-gap junctions, Appl. Phys. Lett. **104**, 221904 (2014).

[31] Zheng Yang, Sean Hart, Changhyun Ko, Amir Yacoby, and Shriram Ramanathan, Studies on electric triggering of the metal-insulator transition in VO_2 thin films between 77 and 300 K, J. Appl. Phys. **110**, 033725 (2011).

[32] Yin Shi, Fei Xue, and Long-Qing Chen, Ginzburg-Landau theory of metal-insulator transition in VO_2: The electronic degrees of freedom, Europhys. Lett. **120**, 46003 (2017).

[33] Yin Shi and Long-Qing Chen, Phase-field model of insulator-to-metal transition in VO_2 under an electric field, Phys. Rev. Mater. **2**, 053803 (2018).

[34] Chris Miller, Mark Triplett, Joel Lammatao, Joonki Suh, Deyi Fu, Junqiao Wu, and Dong Yu, Unusually long free carrier lifetime and metal-insulator band offset in vanadium dioxide, Phys. Rev. B **85**, 085111 (2012).

[35] Anna N. Morozovska, Eugene A. Eliseev, Olexandr V. Varenyk, Yunseok Kim, Evgheni Strelcov, Alexander Tselev, Nicholas V. Morozovsky, and Sergei V Kalinin, Nonlinear space charge dynamics in mixed ionic-electronic conductors: Resistive switching and ferroelectric-like hysteresis of electromechanical response, J. Appl. Phys. **116**, 066808 (2014).

[36] John L. Moll, *Physics of Semiconductors* (McGraw-Hill, New York, 1964).

[37] Long-Qing Chen, Phase-field models for microstructure evolution, Annu. Rev. Mater. Res. **32**, 113 (2002).

[38] Deyi Fu, Kai Liu, Tao Tao, Kelvin Lo, Chun Cheng, Bin Liu, Rong Zhang, Hans A. Bechtel, and Junqiao Wu, Comprehensive study of the metal-insulator transition in pulsed laser deposited epitaxial VO_2 thin films, J. Appl. Phys. **113**, 043707 (2013).

[39] W. H. Rosevear and W. Paul, Hall Effect in VO_2 near the Semiconductor-to-Metal Transition, Phys. Rev. B **7**, 2109 (1973).

[40] Zheng Yang, Changhyun Ko, Viswanath Balakrishnan, Gokul Gopalakrishnan, and Shriram Ramanathan, Dielectric and carrier transport properties of vanadium dioxide thin films across the phase transition utilizing gated capacitor devices, Phys. Rev. B **82**, 205101 (2010).

[41] W. Shockley and W. T. Read, Statistics of the recombinations of holes and electrons, Phys. Rev. **87**, 835 (1952).

[42] Sangwook Lee, Kedar Hippalgaonkar, Fan Yang, Jiawang Hong, Changhyun Ko, Joonki Suh, Kai Liu, Kevin Wang, Jeffrey J. Urban, Xiang Zhang, Chris Dames, Sean A. Hartnoll, Olivier Delaire, and Junqiao Wu, Anomalously low electronic thermal conductivity in metallic vanadium dioxide, Science **355**, 371 (2017).

[43] D. Lee *et al.*, Isostructural metal-insulator transition, Science **362**, 1037 (2018).